Quantitative Study of the Photothermal Properties of Metallic Nanowire Networks

Alan P. Bell,[†,§,⊥] Jessamyn A. Fairfield,[†,§,⊥] Eoin K. McCarthy,[§] Shaun Mills,[†,§,⊥] John J. Boland,[†,§,⊥] Guillaume Baffou,[∥] and David McCloskey[*,‡,§,⊥]

[†]School of Chemistry, [‡]School of Physics, [§]Centre for Research on Adaptive Nanostructures and Nanodevices (CRANN), and [⊥]AMBER Research Centre, Trinity College Dublin, Dublin 2, Ireland and [∥]Institut Fresnel, UMR 7249, CNRS, Aix Marseille Université, Centrale Marseille, 13013 Marseille, France

ABSTRACT In this article, we present a comprehensive investigation of the photothermal properties of plasmonic nanowire networks. We measure the local steady-state temperature increase, heat source density, and absorption in Ag, Au, and Ni metallic nanowire networks under optical illumination. This allows direct experimental confirmation of increased heat generation at the junction between two metallic nanowires and stacking-dependent absorption of polarized light. Due to thermal collective effects, the local temperature distribution in a network is shown to be completely delocalized on a micrometer scale, despite the nanoscale features in the heat source density. Comparison of the experimental temperature profile with numerical simulation allows an upper limit for the effective thermal conductivity of a Ag nanowire network to be established at 43 Wm^{-1} K^{-1} (0.1 κ_{bulk}).

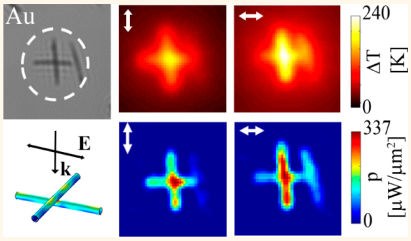

KEYWORDS: thermoplasmonics · nanowire networks · temperature microscopy · nanowelding

Photothermal properties of plasmonic nanoparticles have generated much interest over the past decade, resulting in the development of many novel techniques and technologies including photothermal cancer therapy,[1−3] photoacoustic tomography,[4] local drug release,[5] nanosurgery,[6,7] microfluidics,[8] manipulation of cell adhesion,[9] local superheating,[10] and heat-assisted magnetic recording.[11] Many nanoparticles of various compositions, morphologies, and sizes have been investigated in order to estimate and compare their capabilities as efficient nanoscale sources of heat under illumination. While spherical gold nanoparticles are best suited for applications under visible illumination (unless agglomerated),[12] gold nanoshells[13,14] and nanorods[15] are excellent candidates for biomedical applications due to their tunable near-infrared plasmonic resonance lying within the transparency window of biological tissue.

Despite studies of a wide variety of plasmonic nanoparticles, the photothermal properties of metallic nanowires have not been so widely investigated. Chemically synthesized nanowires can be mass produced and have an extremely large aspect ratio and surface to volume ratio, which is expected to yield singular thermal properties. Large quantities of these nanowires can be easily deposited on a surface using spray deposition or spin-coating techniques.[16] The resulting nanowire networks exhibit specific electrical,[17−19] optical,[20] and physical[21] properties, which are in general controlled by the properties of the constituent junctions. Nanowire networks can be used to fabricate transparent flexible conductors, strain sensors,[12] self-healing materials,[22] improved solar cells,[23] and artificial skin.[24,25]

Nanowire networks can be considered as a random ensemble of individual nanoparticles or as an effective film with considerably reduced thermal conductivity. In ensembles or networks of plasmonic structures, the local temperature at a nanoparticle depends on the density of nanoparticles (heat sources) in the surrounding area. Two distinct regimes are observed, where the temperature increase is either localized around each nanoparticle or completely delocalized across the array.[26] Indeed, thermoplasmonic related experiments very rarely concern single-nanoparticle heating, and heating many nanoparticles at a time can lead to

* Address correspondence to mccloskd@tcd.ie.

Received for review March 18, 2015 and accepted May 4, 2015.

Published online May 04, 2015
10.1021/acsnano.5b01673

unexpected temperature profiles in the surrounding medium.[27,28]

In this article, we present a comprehensive investigation of the photothermal properties of plasmonic nanowire networks. To fully understand heating in such systems, we initially focus on the simple case of isolated metallic nanowires, made of gold, silver, and nickel, and detail their polarization-dependent absorption. Subsequently, we investigate heat generation and temperature confinement at discrete nanowire junctions and their stacking-dependent absorption. Finally, we investigate complex networks of randomly orientated connected nanowires and discuss delocalization and scaling of the local temperature distribution.

RESULTS AND DISCUSSION

Theoretical Background. Electromagnetically induced heating in metals is predominantly the result of the Joule effect. This process is proportional to the square of the electric field inside the metal and the intrinsic material losses of the metal. In a general form, the volumetric heat source density $q(\mathbf{r})$ [W/m^3] generated inside the metal is given by[29]

$$q(\mathbf{r}) = (\omega/2)\mathrm{Im}(\varepsilon)|\mathbf{E}(\mathbf{r})|^2 \quad (1)$$

where ω is the angular frequency of the incident light, ε is the frequency-dependent permittivity of the metal which determines the local response of the electrons to the external field, and $\mathbf{E}$ is the electric field in the metal. All of the material loss mechanisms, including interband transitions, are contained within the imaginary component of the permittivity. The total power absorbed by a nanoparticle, P_{abs} [W], is then given by the integral of the volumetric heat source density over the volume of the particle

$$P_{abs} = \int_{sw} q(\mathbf{r})\mathrm{d}\mathbf{r} \quad (2)$$

Under optical illumination, the metallic nanoparticle will thermally equilibrate internally on a fast time scale, which depends on particle size, and reach a stable thermal equilibrium with the surrounding medium on a longer time scale determined by the thermal diffusivity of the surrounding media. Typical time scales for a nanoparticle in water are on the order of nanoseconds for internal thermal equilibrium and microseconds for equilibrium with the surrounding media.[30] Under illumination and in the steady state, the inner nanoparticle temperature distribution $T(\mathbf{r})$ is governed by the Poisson equation

$$\kappa\nabla^2 T(\mathbf{r}) = -q(\mathbf{r}) \quad (3)$$

where κ is the constant thermal conductivity of the metal and $q(\mathbf{r})$ is the volumetric heat source density in the nanowire. Outside the nanoparticle, the temperature distribution is governed by the Laplace equation:

$$\nabla^2 T(\mathbf{r}) = 0 \quad (4)$$

Experimental Background. The experimental local steady-state temperature measurements were performed using a recently developed technique named TIQSI for thermal imaging using quadriwave shearing interferometry.[31] In brief, the samples are immersed in glycerol, and a plane wave crosses the region of interest, undergoing a distortion due to the thermally induced variation of the refractive index in the glycerol. This wavefront distortion is imaged using a QSI wavefront sensor and then processed using an inversion algorithm to retrieve both the local temperature increase (δT [K]) and the 2D heat source density (p [μW/μm^2]) with submicrometric spatial resolution (~400 nm). The 2D heat source density $p(x,y)$ measured with this technique is defined as the integral of the 3D heat source density q over the thickness of the wire. Interestingly, integration of the experimental maps of $p(x,y)$ over x and y allows quantitative measurement of the total power absorbed (or equivalently delivered) by the composite nanoparticle.[32] Dividing this integral by the incident irradiance I_0 gives an expression for absorption cross section, $\sigma_{abs}[m^2]$, which is a common metric to define the absorption strength of a nanoparticle

$$\sigma_{abs} = \frac{1}{I_0}\int p(x,y)\mathrm{d}x\mathrm{d}y \quad (5)$$

TIQSI therefore provides a powerful noninvasive technique to recover the local steady-state temperature increase, the heat source density, and the absorption cross sections of nanoscale particles with arbitrary geometry, like the complex nanowire system investigated herein.

Single Nanowires. Initially, we investigated heating in single isolated Au, Ag, and Ni nanowires. These nanowires show a strong frequency- and polarization-dependent absorption due to the excitation of localized surface plasmons (LSP) transverse to the wire axis (Supporting Information Figure S2). Without loss of generality, we can consider two cases (depicted in Figure 1a) of incident light linearly polarized along the nanowire axis, referred to as the transverse magnetic case (TM), and light polarized perpendicular to the axis, referred to as the transverse electric case (TE). The response for arbitrary incident polarization can be calculated as a linear combination of these two cases. The finite element method (FEM) is employed to numerically calculate the internal electric field in the nanowire under optical illumination, which is then converted to the heat source density using eq 1. Figure 1b shows the heat source density distribution for a 60 nm diameter Au nanowire illuminated with a free space wavelength of 532 nm. The effect of the LSP is to increase the internal field and therefore the heat generation at the resonant frequency for the TE-polarized case and not for the TM case. Figure 1c shows an optical image of a single Au nanowire with a 10 μm length. The nanowire appears dark in transmission and is quite visible despite nanoscale lateral dimensions due to its

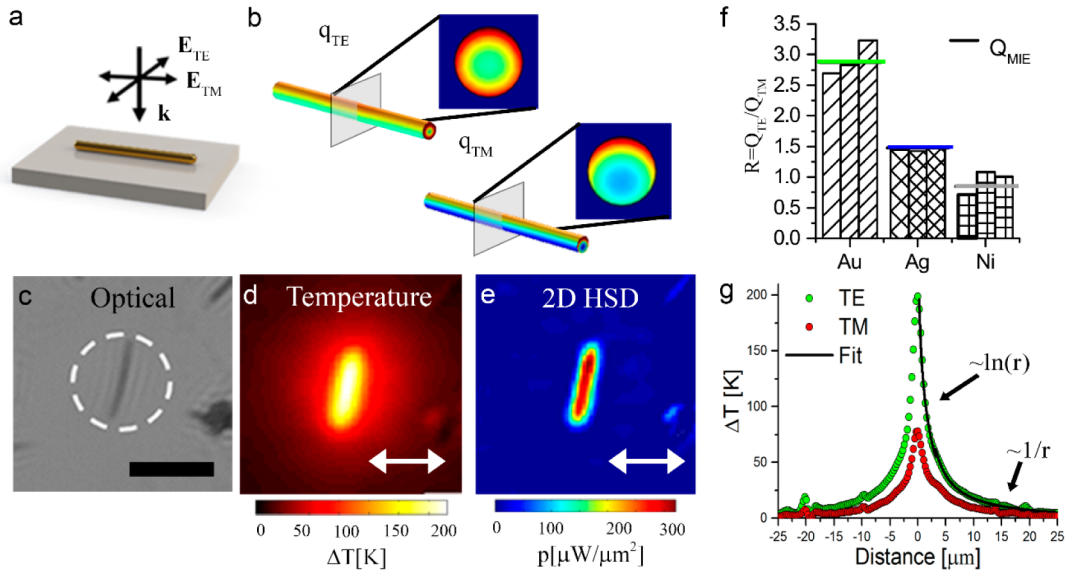

Figure 1. (a) Schematic of TE and TM cases of incident excitation for a single nanowire. (b) Numerically calculated volumetric heat source density distribution $q(r)$ for TE and TM cases on a single Au nanowire with a 60 nm diameter. (c) Optical image in transmission of a single Au nanowire. Dashed circle shows the illumination area. Scale bar is 10 μm. (d) Experimentally measured steady-state temperature distribution under illumination intensity of I_0 = 2.82 mW/μm^2 for the TE case. Incident polarization inset. (e) Experimentally measured 2D heat source density distribution $p(r)$ for same wire. (f) Ratio of heating $R = \sigma_{abs}^{TE}/\sigma_{abs}^{TM}$ for the TE and TM cases. Columns represent experimental measurements on three distinct nanowires. The solid lines are the predicted ratios from Mie theory. (g) Cross section of experimentally measured temperature distribution for TE and TM incident polarization. The temperature distribution shows a ln(r) dependence close to the nanowire, as expected from an infinite wire, and a 1/r dependence at further distances due to its finite length.

large scattering and absorption cross section and blurring from the diffraction limit of the collection objective (NA = 1.4). The excitation area is shown as a white dashed line. Figure 1d shows the measured steady-state temperature distribution with incident irradiance I_0 = 2.82 mW/μm^2 for TE incident polarization. This intensity is sufficient to induce significant heating in the nanowire leading to a temperature increase of 200 K. The 2D heat source density (p [μW/μm^2]) distribution can be extracted (Figure 1e), showing as expected that the heat is delivered uniformly along the length of the nanowire. Integration of this heat source density in accordance with eq 5 gives an absorption cross section for the nanowire of σ_{abs}^{TE} = 0.71 μm^2 for TE polarization compared to σ_{abs}^{TM} = 0.35 μm^2 for TM polarization.

To experimentally quantify the polarization-dependent absorption in the nanowires, the ratio of the steady-state temperatures under fixed excitation intensity for TE and TM illumination was measured for a range of distinct nanowires. For these extremely high aspect ratio wires, the LSP is only effectively excited when the incident light is polarized perpendicular to the nanowire axis (TE case). Therefore, a comparison of TE to TM heating is the most precise way to quantify the contribution of LSP to the heating. At an excitation wavelength of 532 nm, the Au nanowires show the most anisotropy due to the frequency dependence of the LSP resonance, with a ratio $R = \sigma_{abs}^{TE}/\sigma_{abs}^{TM}$ of 3. The ratio is R = 1.5 for Ag nanowires and R = 1 for Ni. The wavelength dependence of this ratio calculated from Mie theory for an infinite cylinder is plotted in Figure S3. Figure 1f compares experimental values of R (columns) for three different Au, Ag, and Ni nanowires with the calculated ratios from the Mie theory solution (solid lines). Single metallic nanowires can also support propagating surface plasmon polariton (SPP) modes, which can be excited at a discontinuity such as the finite end of the nanowire, allowing their use as nanoscale waveguides.[33] To study the contribution of these SPP modes to the total absorption cross section, we conducted 3D FEM simulations. The intensity enhancement (Figure S5a) and heat source density (Figure S5c) for a 30 nm radius infinite Ag wire are compared with that of a semi-infinite wire with a spherically capped 30 nm radius (Figure S5b,d). The relative heat source density normalized to Mie theory for an infinite wire shows that the launched SPP modes contribute to increased heating in only the first 250 nm of the wire. The wire is in a symmetric environment (glycerol and glass with similar refractive index), so it is difficult to efficiently match the momentum required to launch a bound SPP mode in the nanowire. This sharp 250 nm falloff can be attributed to launching of lossy modes in the wire. The total contribution of SPPs to the absorption cross section can be seen by plotting the cumulative difference of the heating in the finite wire to that in an infinite wire in Figure S5f and is less than 7% for a 1 μm long wire. The agreement of the ratio of measured absorption cross sections with Mie theory, which is for an infinitely long nanowire, demonstrates that although it is possible to excite SPPs at the nano-

wire ends, they do not contribute significantly to the polarization response of heat generation.

A cross section of the steady-state temperature distribution through the center of a Au nanowire perpendicular to the nanowire axis is shown in Figure 1g for TE (green dots) and TM (red dots) illumination. For a wire with a uniform volumetric heat source density, the temperature distribution shows a ln(**r**) dependence close to the nanowire, as expected from an infinite wire, and a 1/**r** dependence at further distances due to its finite length. The solid line in Figure 1g shows the temperature profile is well-fitted with a logarithmic falloff in the first 5 μm with a 1/**r** dependence afterward. This demonstrates that a single nanowire can create a temperature increase which is localized to a full width at half-maximum (fwhm) of 2.2 μm in the glycerol, with a thermal gradient (which depends on incident power) on the order of 95 K/μm. Measurements of temperature distributions and heat source densities were taken for multiple nanowires and junctions on each sample. For brevity, only a few selected results were shown in the main text; however, given the speed and simplicity of the technique, a large number of nanowire samples were investigated (see Figure S6). Table 1 summarizes results comparing heating in single Au, Ag, and Ni nanowires.

TABLE 1. Summarized Results for Single Nanowires with D = 60 nm and L = 10.1 μm

	σ_{abs} (EXP) [μm^2]		σ_{abs} (MIE) [μm^2]		σ_{abs} (FEM) [μm^2]	
	TM	TE	TE	TM	TE	TM
Au	0.71	0.35	0.82	0.22	0.82	0.23
Ag	0.21	0.14	0.08	0.06	0.07	0.05
Ni	0.45	0.48	0.38	0.48	0.39	0.56

		I/I_0 (FEM)		ΔT [K]	
	I_0 [mW/μm^2]	TE	TM	TM	TE
Au	2.82	8.98	1.54	203	77
Ag	2.97	8.92	1.79	26	18
Ni	1.79	5.37	1.73	60	67

Nanowire Junctions. Subsequently, we investigated the more complex case of heating at the junction between two nanowires. Recent experimental studies have shown that optical illumination of nanowire networks can significantly increase the film conductivity by induced recrystallization at nanowire junctions referred to as "nanowelding".[34,35] This effect was postulated to be due to enhanced electric fields and heating at nanowire junctions; however, only a numerical investigation of the detailed mechanism was possible.[28] In this work, we quantitatively measure the heat source density at a junction between two nanowires, providing direct evidence of enhanced heating. Single-nanowire junctions of Au, Ag, and Ni were investigated for two orthogonal cases of incident polarization. An optical image of the junction and illuminated area and the 2D heat source density maps for two orthogonal polarizations are displayed in Figure 2a–c for Au, Ag, and Ni, respectively. The results clearly demonstrate a localized hot spot in the heat source density at the intersection for the nanowires for all three metals. The polarization dependence shows a distinct asymmetry in that one nanowire will contribute significantly more to the heating for a particular incident polarization, most evident in the case of the Au nanowires with an excitation wavelength

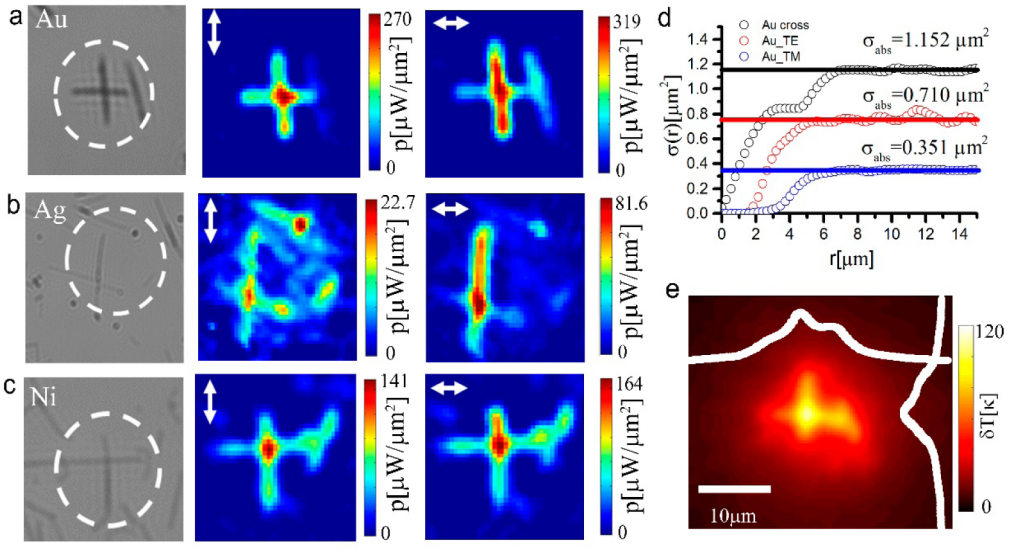

Figure 2. Optical images and heat source density maps, p, for different incident polarizations on single-nanowire junctions for (a) Au, (b) Ag, and (c) Ni nanowires. (d) Integrating the 2D heat source densities radially from the center point of the junction allows quantitative measurement of the absorption cross section. Plotted is the cumulative integral for the Au cross in (a) compared to a single Au wire under TE and TM polarization. (e) Temperature map for the Ni nanowire junction from (c) with incident light polarized along the x axis. The spreading of the temperature profile is determined by the thermal conductivity of the surrounding media. Overlays show cross sections of the temperature profile through the center of the junction.

of 532 nm. The experimentally mapped 2D heat source density is numerically integrated to attain the total absorption cross section of the nanowire junction. To accurately determine this value, the integration is performed radially starting from the geometric center of the illuminated area. The cumulative integration is shown as a function of radius in Figure 2d. The total absorption cross section is then determined as the value at which the cumulative integration levels off. In the case of the Au nanowire junction shown in Figure 2a, integration of the experimentally mapped 2D heat source density, p, yields an absorption cross section of $\sigma_{abs} = 1.15 \pm 0.02\ \mu m^2$, which is only marginally larger than that of two isolated nanowires ($\sigma_{abs}^{TE} = 0.71 \pm 0.02\ \mu m^2$, $\sigma_{abs} = 0.35 \pm 0.02\ \mu m^2$) due to heat source density enhancement at the junction. The two intersecting nanowires can be thought of as a composite nanoparticle, which has increased absorption cross section from a single nanowire.[36] Figure 2e shows that the temperature increase of 120 K can be reached at a Ni nanowire junction with an irradiance of 1.32 mW/μm^2. The spreading of the temperature distribution compared to the heat source density depends on the thermal conductivity of the surrounding medium. For completeness, a wider selection of thermal maps related to various nanowire configurations is presented in Supporting Information (Figure S7).

The polarization dependence of the heat source density of the nanowire junctions can be explained by considering the stacking of the nanowires. We can identify two cases as depicted in Figure 3: case 1, where the incident polarization is perpendicular (TE) to the top nanowire, and case 2, where the incident polarization is along the axis (TM) of the top nanowire. We use three-dimensional FEM simulation to examine the local electric field enhancement and the resistive heating profiles. Figure 3 shows the case of 532 nm light incident on 60 nm diameter Ni nanowires with a 4 nm gap between wires at the junction to account for the surface oxide. For both cases, there is an enhancement in the electric field at the gap between the two wires. This electric field enhancement leads to an increase of the electric field inside the nanowires at the junction, which in turn leads to enhanced localized heating. The maximum contrast is achieved for case 1, where the incident polarization is perpendicular to the top nanowire axis. In this case, a LSP is effectively excited in the top nanowire, resulting in a field enhancement of 9.5 times at the junction (Figure 3b,c). For case 2, the top nanowire scatters the incident light, which reduces the LSP effect in the bottom nanowire, leading to a smaller field enhancement of 3.5 times and less contrast in the heating profile (Figure 3f,g).

The 2D heat source density profile is calculated from the FEM results by integrating the 3D heat source density over the z axis. The simulation domain for the FEM was limited to 1 μm × 0.5 μm × 0.5 μm due

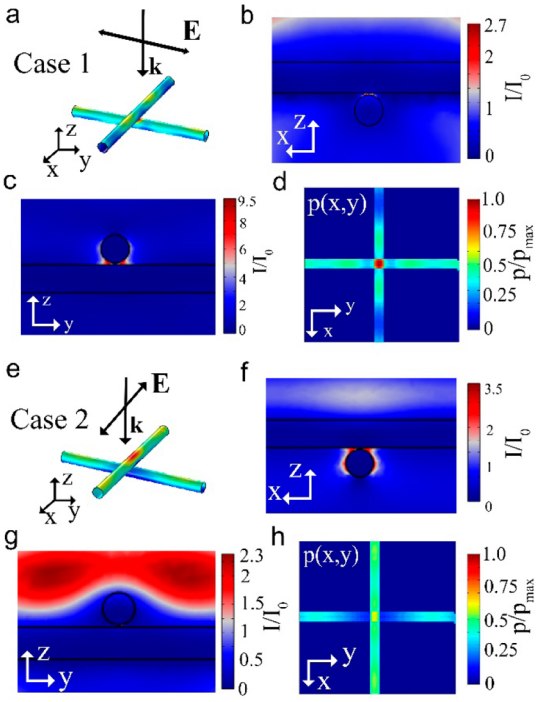

Figure 3. (a) Three-dimensional map of resistive heating distribution in the Ni nanowire junction calculated from FEM. Incident illumination is polarized perpendicular to the top nanowire, termed case 1. (b) Intensity enhancement in the $z-x$ plane through the center of the junction. (c) Intensity enhancement in the $z-y$ plane. (d) Two-dimensional heat source density map obtained from integrating 3D results along the z axis. (e–h) Same as (a–d), but incident light is polarized along the axis of the top nanowire, termed case 2.

to finite computational resources. It is not feasible to simulate the full 10.2 μm using this method, so periodic boundary conditions were used in the $x-y$ directions, with perfectly matched layers in the z direction. The FEM-determined 2D heat source density shows the expected enhanced heat generation at the nanowire junction; however, the absolute value of the 2D heat source density cannot be directly compared with the longer experimentally measured nanowires of Figure 2. The experimental results are also convolved with the point spread function of the collection objective. SPPs excited at this junction may provide an additional absorption mechanism to increase the absorption cross section of the composite particle, but this effect will be included in the experimentally measured cross sections and FEM simulations. In both excitation cases, larger heating is observed in the TE-illuminated nanowire, consistent with previous predictions in silver nanowires.[18] The stacking dependence of the heat source density in the FEM simulations explains the polarization dependence observed in the experimental measurements. Table 2 summarizes results comparing heating in single Au, Ag, and Ni nanowire junctions.

Nanowire Networks. Finally, we investigated heating in large-scale, fully connected nanowire networks which are physically relevant for applications such as

transparent conductors, flexible electronics, and memristive devices. Nanowire networks can be considered as an ensemble of individual nanowires or as a thin film with considerably reduced effective thermal conductivity. Studies on heating in ensembles of nanoparticles reveal that the steady-state temperature distribution can be strongly localized around each nanoparticle or, conversely, completely uniform throughout the system, depending on nanoparticle coverage[37,38] on the substrate.

To quantitatively investigate the local temperature increase in nanowire network systems, we map the temperature distribution of a Ag nanowire network under different optical excitation conditions. A 40× objective and a variable aperture were employed to achieve illumination of the network over two distinct circular areas with diameters of D = 50 and 100 μm. Scattered light optical images are shown in Figure 4a,b, with the illumination area identified using a white circle. The laser power was controlled to maintain constant intensity on the sample, I = 0.127 mW/μm^2 (Figure 4b,c). Profiles of the local temperature along a line through the center of the illuminated area are shown in Figure 4d. The experimental temperature maps (Figure 4c,d) and profiles (Figure 4e) demonstrate that, at a nanowire density physically relevant for transparent conductors, the temperature increase is fully delocalized on the micrometric scale throughout the network despite a contrasted heat source density on the nanoscale. The total power absorbed in the network can be found by integrating the heat source density. We find that the silver nanowire network absorbs only a small fraction (0.4%) of the incident power at this network density and wavelength. This is 10% of the power that would be absorbed by a 60 nm thick continuous Ag film. Note that TIQSI allows a quantitative measurement of absorbed power not an approximate absorption measurement by transmission measurement.

In contrast to the steady-state temperature surrounding a finite collection of nanoparticles, the local temperature reached for a thin film depends on the thermal conductivity of the film. A high thermal conductivity will spread the energy, resulting in a lower steady-state temperature increase in the center of the illumination area and a smaller temperature gradient (Figure S6). Using the experimentally measured absorbed power as a source term for a 3D FEM thermal simulation, we find that, in order to match experimental results, we must use a thin film thermal conductivity less than 43 Wm^{-1} K^{-1}, which is 10% that of a bulk silver film (429 Wm^{-1} K^{-1}). This is defined as an upper limit for the thermal conductivity of the effective film, as the dependence of the steady-state temperature distribution ceases when the thermal conductivity of the film is less than that of the surrounding media (Figure S6). The dashed lines in Figure 4e show the FEM results with the effective thin film thermal conductivity. Deviations from the ideal case are due to density

TABLE 2. Summarized Results for Nanowire Junctions

		I/I_0 (FEM)	
	I_0 [mW/μm^2]	case 1	case 2
Au	0.63	106	58
Ag	2.82	80.4	37.8
Ni	1.65	7.85	9.3

	σ_{abs} (EXP) [μm^2]		ΔT [K]	
	case 1	case 2	case 1	case 2
Au	1.13	1.08	120	110
Ag	0.21	0.19	25	23
Ni	0.92	0.83	110	102

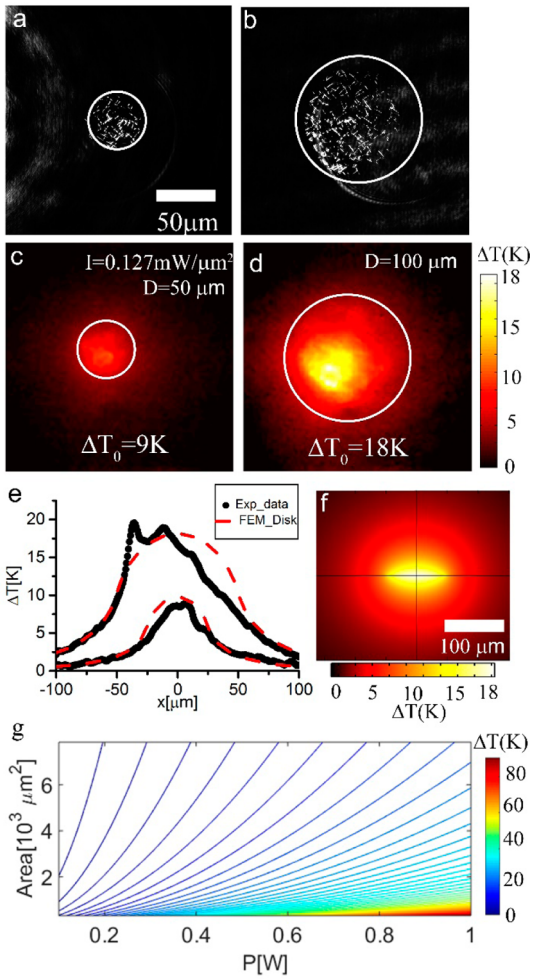

Figure 4. Scattered light images of the excitation laser depicting the illuminated areas of diameter (a) D = 50 μm and (b) D = 100 μm. (c,d) Experimental temperature maps taken at constant irradiance. (e) Cross section of temperature map through the center of the illumination region. Dashed red lines show FEM simulation of the temperature distribution. (f) Out-of-plane temperature map calculated from 3D FEM. (g) Contour plot of isotherms in the incident power and illumination area parameter space. Results show careful consideration of both incident power and illumination area required to accurately determine the local temperature increase.

variations in the network, which correlate well with the images in Figure 4a,b.

The delocalization of temperature across the nanowire network has important implications for controlling the local steady-state temperature increase under optical illumination. Experimental measurements were performed at different incident powers and illumination areas (Figure S6). The maximum temperature increase, T_0, is shown to scale linearly with the diameter of the illuminated D area according to $T_0 \propto DI$ or equivalently $T_0 \propto P/D$. This is what would be expected for a 2D circular heat source.[26] This important fact means that to appropriately scale the incident power to maintain a constant temperature at the interface, the illuminated area needs to be considered. To illustrate this fact, the isotherms of local temperature are plotted over the incident power and illumination area parameter space in Figure 4g. Using this experimental calibration, we can now know the local steady-state temperature for any incident power and illumination area (accounting for density variations in the network). This is an important calibration as the local temperature increase is needed in order to make quantitative comparisons between the efficacy of thermally (hot plate),[37] electrically,[38] and optically[35] induced increase of conductivity in nanowire transparent conductors. We show that both the incident power and illumination area are required to determine the actual temperature at the sample. Specification of the size of the illuminated area is often omitted in reported experimental studies in thermoplasmonics.

CONCLUSIONS

We directly measure the optically induced local temperature increase, heat source density, and absorption cross sections in nanowire systems of varying complexity. We directly observe enhanced heat generation at the junction between two single nanowires, an effect which previously has only been postulated numerically. We show that this temperature localization exists even for nickel nanowires, which have a strongly damped plasmonic resonance. The polarization dependence of heating in a single-nanowire junction is explained as resulting from the stacking order. The temperature distribution in a Ag nanowire network is shown to be delocalized and scale linearly with the diameter of the illuminated region. From this scaling, we can calibrate the local temperature increase at the surface for different powers and illumination areas. For nanowire networks, we show that, due to thermal collective heating, it is imperative to consider the illuminated area in order to accurately determine the local steady-state temperature reached. An upper limit for the effective thermal conductivity of a Ag nanowire network is given as 43 Wm^{-1} K^{-1} by comparison of the steady-state temperature profile with numerical FEM simulations. This work provides quantitative measurements to aid in interpretation of thermally induced effects in nanowire systems such as nanowelding for transparent conductors and nanowire networks, filament formation in nickel nanowire networks,[39] and film heaters.[40] Previous studies were unable to quantitatively measure optically induced local temperature increase, making comparison between optically induced heating and thermally induced heating (*e.g.*, using a hot plate) qualitative. This work contributes to understanding heat generation and dissipation in nanoscale systems, which is of major importance for further scaling of electronic devices and development of new nanotechnologies.

METHODS

Nanowire Network Preparation. Experimental samples were formed by spray deposition of commercially available single-crystalline gold (Sigma-Aldrich), silver (Seashell Technology), and nickel (Nanomaterials.it) nanowires onto quartz substrates. The density of the nanowire distribution was controlled to either have a predominance of single nanowires, isolated nanowire junctions/crossings, or fully connected nanowire films. The Au nanowires have a passivation monolayer of cetyltrimethylammonium bromide to avoid aggregation in solution, whereas the Ag nanowires have a 3 nm thick dielectric surface coating of poly(vinylpyrrolidone). The Ni wires have a 5 nm surface oxide layer. Statistical analysis of TEM and SEM imaging confirmed an average diameter D (length L) of 50 nm (8 μm) for the Au nanowires, 90 nm (7.3 μm) for Ag, and 80 nm (9.4 μm) for Ni (see Supporting Information Figure S1).

Thermal Imaging Using Quadriwave Shearing Interferometry (TIQSI). Experimental heating measurements were performed using a 532 nm diode-pumped solid-state laser (10 W Millenia, SpectraPhysics) as the thermal excitation source. The laser was expanded onto a variable iris in the image plane of the objective to produce a top hat intensity distribution on the sample over a 10.2 μm diameter area. The laser power was then varied to control the incident irradiance. A red LED array source is used as the plane wave source for phase mapping. A detailed explanation of the TIQSI technique is given in ref 31.

Conflict of Interest: The authors declare no competing financial interest.

Acknowledgment. The authors wish to acknowledge funding from the European Research Council under Advanced Grant 321160. This publication has emanated from research supported in part by a research grant from Science Foundation Ireland (SFI) under Grant Number SFI/12/RC/2278. J.A.F. acknowledges funding from the Irish Research Council EMPOWER Fellowship. The travel in this work was made possible through the Irish Research Council ULYSSES travel grant. G.B. acknowledges financial support from the Agence Nationale de la Recherche (ANR) grant NATO (ANR-13-BS10-0013).

Supporting Information Available: TEM images and statistical analysis of diameter and length distributions of nanowires used. Further experimental and numerical results are provided. The Supporting Information is available free of charge on the ACS Publications website at DOI: 10.1021/acsnano.5b01673.

REFERENCES AND NOTES

1. Ayala-Orozco, C.; Urban, C.; Bishnoi, S.; Urban, A.; Charron, H.; Mitchell, T.; Shea, M.; Nanda, S.; Schiff, R.; Halas, N.; et al. Sub-100nm Gold Nanomatryoshkas Improve Photothermal Therapy Efficacy in Large and Highly Aggressive

Triple Negative Breast Tumors. *J. Controlled Release* **2014**, *191*, 90–97.
2. Ayala-Orozco, C.; Urban, C.; Knight, M. W.; Urban, A. S.; Neumann, O.; Bishnoi, S. W.; Mukherjee, S.; Goodman, A. M.; Charron, H.; Mitchell; et al. Au Nanomatryoshkas as Efficient Near-Infrared Photothermal Transducers for Cancer Treatment: Benchmarking against Nanoshells. *ACS Nano* **2014**, *8*, 6372–6381.
3. Gobin, A. M.; Lee, M. H.; Halas, N. J.; James, W. D.; Drezek, R. A.; West, J. L. Near-Infrared Resonant Nanoshells for Combined Optical Imaging and Photothermal Cancer Therapy. *Nano Lett.* **2007**, *7*, 1929–1934.
4. Wang, L. V.; Hu, S. Photoacoustic Tomography: *In Vivo* Imaging from Organelles to Organs. *Science* **2012**, *335*, 1458–1462.
5. Han, G.; Ghosh, P.; De, M.; Rotello, V. M. Drug and Gene Delivery Using Gold Nanoparticles. *Nanobiotechnology* **2007**, *3*, 40–45.
6. Huschka, R.; Barhoumi, A.; Liu, Q.; Roth, J. A.; Ji, L.; Halas, N. J. Gene Silencing by Gold Nanoshell-Mediated Delivery and Laser-Triggered Release of Antisense Oligonucleotide and siRNA. *ACS Nano* **2012**, *6*, 7681–7691.
7. Urban, A. S.; Pfeiffer, T.; Fedoruk, M.; Lutich, A. A.; Feldmann, J. Single-Step Injection of Gold Nanoparticles through Phospholipid Membranes. *ACS Nano* **2011**, *5*, 3585–3590.
8. Donner, J. S.; Baffou, G.; McCloskey, D.; Quidant, R. Plasmon-Assisted Optofluidics. *ACS Nano* **2011**, *5*, 5457–5462.
9. Zhu, M.; Baffou, G.; Meyerbröker, N.; Polleux, J. Micropatterning Thermoplasmonic Gold Nanoarrays To Manipulate Cell Adhesion. *ACS Nano* **2012**, *6*, 7227–7233.
10. Baffou, G.; Polleux, J.; Rigneault, H.; Monneret, S. Super-heating and Micro-bubble Generation around Plasmonic Nanoparticles under CW Illumination. *J. Phys. Chem. C* **2014**, *118*, 4890–4898.
11. Challener, W. A.; Peng, C.; Itagi, A. V.; Karns, D.; Peng, W.; Peng, Y.; Yang, X.; Zhu, X.; Gokemeijer, N. J.; Hsia, Y. T.; et al. Heat-Assisted Magnetic Recording by a Near-Field Transducer with Efficient Optical Energy Transfer. *Nat. Photonics* **2009**, *3*, 220–224.
12. Hutter, E.; Fendler, J. H. Exploitation of Localized Surface Plasmon Resonance. *Adv. Mater.* **2004**, *16*, 1685–1706.
13. Prodan, E.; Radloff, C.; Halas, N. J.; Nordlander, P. A Hybridization Model for the Plasmon Response of Complex Nanostructures. *Science* **2003**, *302*, 419–422.
14. Cole, J. R.; Mirin, N. A.; Knight, M. W.; Goodrich, G. P.; Halas, N. J. Photothermal Efficiencies of Nanoshells and Nanorods for Clinical Therapeutic Applications. *J. Phys. Chem. C* **2009**, *113*, 12090–12094.
15. Link, S.; El-Sayed, M. A. Spectral Properties and Relaxation Dynamics of Surface Plasmon Electronic Oscillations in Gold and Silver Nanodots and Nanorods. *J. Phys. Chem. B* **1999**, *103*, 8410–8426.
16. Scardaci, V.; Coull, R.; Lyons, P. E.; Rickard, D.; Coleman, J. N. Spray Deposition of Highly Transparent, Low-Resistance Networks of Silver Nanowires over Large Areas. *Small* **2011**, *7*, 2621–2628.
17. Bellew, A. T.; Bell, A. P.; McCarthy, E. K.; Fairfield, J. A.; Boland, J. J. Programmability of Nanowire Networks. *Nanoscale* **2014**, *6*, 9632–9639.
18. Fairfield, J. A.; Ritter, C.; Bellew, A. T.; McCarthy, E. K.; Ferreira, M. S.; Boland, J. J. Effective Electrode Length Enhances Electrical Activation of Nanowire Networks: Experiment and Simulation. *ACS Nano* **2014**, *8*, 9542–9549.
19. Nirmalraj, P. N.; Bellew, A. T.; Bell, A. P.; Fairfield, J. A.; McCarthy, E. K.; O'Kelly, C.; Pereira, L. F. C.; Sorel, S.; Morosan, D.; Coleman, J. N.; et al. Manipulating Connectivity and Electrical Conductivity in Metallic Nanowire Networks. *Nano Lett.* **2012**, *12*, 5966–5971.
20. Chen, R.; Das, S. R.; Jeong, C.; Khan, M. R.; Janes, D. B.; Alam, M. A. Co-percolating Graphene-Wrapped Silver Nanowire Network for High Performance, Highly Stable, Transparent Conducting Electrodes. *Adv. Funct. Mater.* **2013**, *23*, 5150–5158.
21. McCarthy, E. K.; Bellew, A. T.; Sader, J. E.; Boland, J. J. Poisson's Ratio of Individual Metal Nanowires. *Nat. Commun.* **2014**, *5*, 4336.
22. Gong, C.; Liang, J.; Hu, W.; Niu, X.; Ma, S.; Hahn, H. T.; Pei, Q. A Healable, Semitransparent Silver Nanowire–Polymer Composite Conductor. *Adv. Mater.* **2013**, *25*, 4186–4191.
23. Langley, D. P.; Giusti, G.; Lagrange, M.; Collins, R.; Jiménez, C.; Bréchet, Y.; Bellet, D. Silver Nanowire Networks: Physical Properties and Potential Integration in Solar Cells. *Sol. Energy Mater. Sol. Cells* **2014**, *125*, 318–324.
24. Boland, J. J. Flexible Electronics: Within Touch of Artificial Skin. *Nat. Mater.* **2010**, *9*, 790–792.
25. Takei, K.; Takahashi, T.; Ho, J. C.; Ko, H.; Gillies, A. G.; Leu, P. W.; Fearing, R. S.; Javey, A. Nanowire Active-Matrix Circuitry for Low-Voltage Macroscale Artificial Skin. *Nat. Mater.* **2010**, *9*, 821–826.
26. Baffou, G.; Berto, P.; Bermúdez Ureña, E.; Quidant, R.; Monneret, S.; Polleux, J.; Rigneault, H. Photoinduced Heating of Nanoparticle Arrays. *ACS Nano* **2013**, *7*, 6478–6488.
27. Baffou, G.; Urena, E. B.; Berto, P.; Monneret, S.; Quidant, R.; Rigneault, H. Deterministic Temperature Shaping Using Plasmonic Nanoparticle Assemblies. *Nanoscale* **2014**, *6*, 8984–8989.
28. Sanchot, A.; Baffou, G.; Marty, R.; Arbouet, A.; Quidant, R.; Girard, C.; Dujardin, E. Plasmonic Nanoparticle Networks for Light and Heat Concentration. *ACS Nano* **2012**, *6*, 3434–3440.
29. Landau, L. D.; Lifšic, E. M.; Pitaevskii, L. P. *Electrodynamics of Continuous Media*; Pergamon Press: Elmsford, NY, 1960; Vol. 364.
30. Baffou, G.; Rigneault, H. Femtosecond-Pulsed Optical Heating of Gold Nanoparticles. *Phys. Rev. B* **2011**, *84*, 035415.
31. Baffou, G.; Bon, P.; Savatier, J.; Polleux, J.; Zhu, M.; Merlin, M.; Rigneault, H.; Monneret, S. Thermal Imaging of Nanostructures by Quantitative Optical Phase Analysis. *ACS Nano* **2012**, *6*, 2452–2458.
32. Berto, P.; Ureña, E. B.; Bon, P.; Quidant, R.; Rigneault, H.; Baffou, G. Quantitative Absorption Spectroscopy of Nano-objects. *Phys. Rev. B* **2012**, *86*, 165417.
33. Lal, S.; Hafner, J. H.; Halas, N. J.; Link, S.; Nordlander, P. Noble Metal Nanowires: From Plasmon Waveguides to Passive and Active Devices. *Acc. Chem. Res.* **2012**, *45*, 1887–1895.
34. Han, S.; Hong, S.; Ham, J.; Yeo, J.; Lee, J.; Kang, B.; Lee, P.; Kwon, J.; Lee, S. S.; Yang, M.-Y.; et al. Flexible Electronics: Fast Plasmonic Laser Nanowelding for a Cu-Nanowire Percolation Network for Flexible Transparent Conductors and Stretchable Electronics. *Adv. Mater.* **2014**, *26*, 5888–5888.
35. Garnett, E. C.; Cai, W.; Cha, J. J.; Mahmood, F.; Connor, S. T.; Greyson Christoforo, M.; Cui, Y.; McGehee, M. D.; Brongersma, M. L. Self-Limited Plasmonic Welding of Silver Nanowire Junctions. *Nat. Mater.* **2012**, *11*, 241–249.
36. Verellen, N.; Van Dorpe, P.; Vercruysse, D.; Vandenbosch, G. A. E.; Moshchalkov, V. V. Dark and Bright Localized Surface Plasmons in Nanocrosses. *Opt. Express* **2011**, *19*, 11034–11051.
37. Lee, J.-Y.; Connor, S. T.; Cui, Y.; Peumans, P. Solution-Processed Metal Nanowire Mesh Transparent Electrodes. *Nano Lett.* **2008**, *8*, 689–692.
38. Song, T.-B.; Chen, Y.; Chung, C.-H.; Yang, Y.; Bob, B.; Duan, H.-S.; Li, G.; Tu, K.-N.; Huang, Y.; Yang, Y. Nanoscale Joule Heating and Electromigration Enhanced Ripening of Silver Nanowire Contacts. *ACS Nano* **2014**, *8*, 2804–2811.
39. Mickel, P. R.; Lohn, A. J.; James, C. D.; Marinella, M. J. Isothermal Switching and Detailed Filament Evolution in Memristive Systems. *Adv. Mater.* **2014**, *26*, 4486–4490.
40. Kim, T.; Kim, Y. W.; Lee, H. S.; Kim, H.; Yang, W. S.; Suh, K. S. Uniformly Interconnected Silver-Nanowire Networks for Transparent Film Heaters. *Adv. Funct. Mater.* **2013**, *23*, 1250–1255.